



# Non-Majorana states yield nearly quantized conductance in proximatized nanowires

P. Yu<sup>1</sup>, J. Chen<sup>1</sup>, M. Gomanko<sup>1</sup>, G. Badawy<sup>2</sup>, E. P. A. M. Bakkers<sup>2</sup>, K. Zuo<sup>3</sup>, V. Mourik<sup>4</sup> and S. M. Frolov<sup>1</sup> ✉

**Semiconductor nanowires with proximity-induced superconductivity are leading contenders for manifesting Majorana fermions in condensed matter<sup>1–5</sup>. However, unambiguous detection of these quasiparticles is controversial<sup>6</sup>, and one proposed method is to show that the peak in the conductance at zero applied bias is quantized to the value of  $2e^2/h$  (refs. 7–10). This has been reported previously<sup>11</sup>, but only by probing one end of the device. Yet, if peaks come from Majorana modes, they should be observed at both ends simultaneously. Here we fabricate devices that feature tunnel probes on both ends of a nanowire and observe peaks that are close to the quantized value. These peaks evolve with the tunnel barrier strength and magnetic field in a way that is consistent with Majorana zero modes. However, we only find nearly quantized zero-bias peaks localized to one end of the nanowire, while conductance dips are observed for the same parameters at the other end. We also identify delocalized states near zero magnetic field and at higher electron density, which is not in the basic Majorana regime. These results enable us to lay out procedures for assessing the non-locality of subgap wavefunctions and provide a classification of nanowire bound states based on their localization.**

Electrical conductance that is quantized to units determined by fundamental constants, although counterintuitive in classical physics, has been shown in many different systems where electron transport is dominated by a few one-dimensional (1D) channels. For example, metrologically robust conductance quantization is observed when backscattering of electron waves is suppressed, in edge states of quantum Hall systems<sup>12</sup>. Quantized conductance in ballistic channels is also well established<sup>13</sup>, but it can be scrambled by scattering<sup>14</sup>. Quantization in helical channels, where opposite spin carriers travel in opposite directions, has been predicted theoretically, but so far not found to be robust in experiments<sup>15–18</sup>. Conductance quantization has also been predicted at low transmission in Majorana transport<sup>7–10</sup>, and its observation remains an ongoing effort.

Majorana modes are manifestations of topological superconductivity that can be engineered, among other systems, in semiconductor nanowires with intrinsic spin–orbit coupling by placing them in contact with conventional superconductors and at the same time subjecting them to external magnetic fields<sup>1–5</sup>. Majorana modes possess non-trivial properties that include pinning to zero energy, quantum state delocalization and non-Abelian exchange<sup>19–21</sup>.

Tunnelling into a Majorana bound state would be seen as a zero-bias conductance peak with its height quantized at exactly

$2e^2/h$  (refs. 7–9). However, this quantization does not survive finite temperature<sup>22–25</sup>, finite system size<sup>23</sup> or when tunnelling at zero energy is also allowed into non-Majorana states<sup>26</sup>. Approximate quantization may still be accessible under realistic experimental conditions when tunnel coupling dominates over both temperature and Majorana splitting. A tunnelling-rate-independent conductance is then expected at a nearly quantized level<sup>10</sup>. However, a recent theory proposed that approximate conductance quantization may be achieved without Majorana modes by fine-tuning trivial low-energy states<sup>27</sup>.

In this Letter, we fabricate three-terminal InSb nanowire devices in the Majorana configuration, allowing tunnelling measurements across both nanowire ends. On the left side, a zero-bias conductance peak (ZBCP) with nearly  $2e^2/h$  absolute conductance appears at finite magnetic field and persists over a considerable field range. This ZBCP is also persistent upon tunnel barrier tuning and only appears when the magnetic field is pointing along the nanowire, all of which is consistent with Majorana theory. However, we do not observe an accompanying peak at the right end of the nanowire at identical settings. Given the NbTiN superconductor-covered nanowire segment length of 400 nm, exceeding the nanowire diameter only by a factor of four, little space is left to locate the second Majorana away from the right end. This rules out the possibility that the observed nearly quantized ZBCPs are due to well-separated Majorana bound states. Instead, we attribute the left ZBCP to topologically trivial Andreev bound states localized on the left end of the nanowire. Following a careful search, we do not find correlated transport resonances simultaneously at both ends of the nanowire at finite magnetic fields that are sufficiently large for us to observe Majorana bound states. We find states delocalized between the left and right ends only around zero field and at more positive gate voltages, away from the single-subband regime. They therefore constitute trivial states extending underneath the entire superconducting contact. We conclude that further efforts are required to understand and optimize nanowire devices, while any claim of Majorana bound state observation should be verified in the three-terminal geometry.

Figure 1a shows the three-terminal hybrid device studied here. A metal–organic vapour-phase epitaxy-grown InSb semiconducting nanowire is covered by a NbTiN superconducting contact (S-lead) in the middle and two normal Pd contacts  $N_L$  and  $N_R$  at the ends. Beneath the nanowire, a 400-nm-wide electrostatic gate (S-gate) controls the electron density under the S-lead. We use tunnel gates  $T_L$  and  $T_R$  to create left and right tunnelling barriers and perform tunnelling spectroscopy on both sides simultaneously. A bias voltage is applied to the middle superconductor, while conductances

<sup>1</sup>University of Pittsburgh, Pittsburgh, PA, USA. <sup>2</sup>Eindhoven University of Technology, Eindhoven, The Netherlands. <sup>3</sup>Center for Emergent Matter Science (CEMS), RIKEN, Saitama, Japan. <sup>4</sup>Centre for Quantum Computation and Communication Technologies, School of Electrical Engineering and Telecommunications, UNSW Sydney, Sydney, New South Wales, Australia. ✉e-mail: [frolovsm@pitt.edu](mailto:frolovsm@pitt.edu)

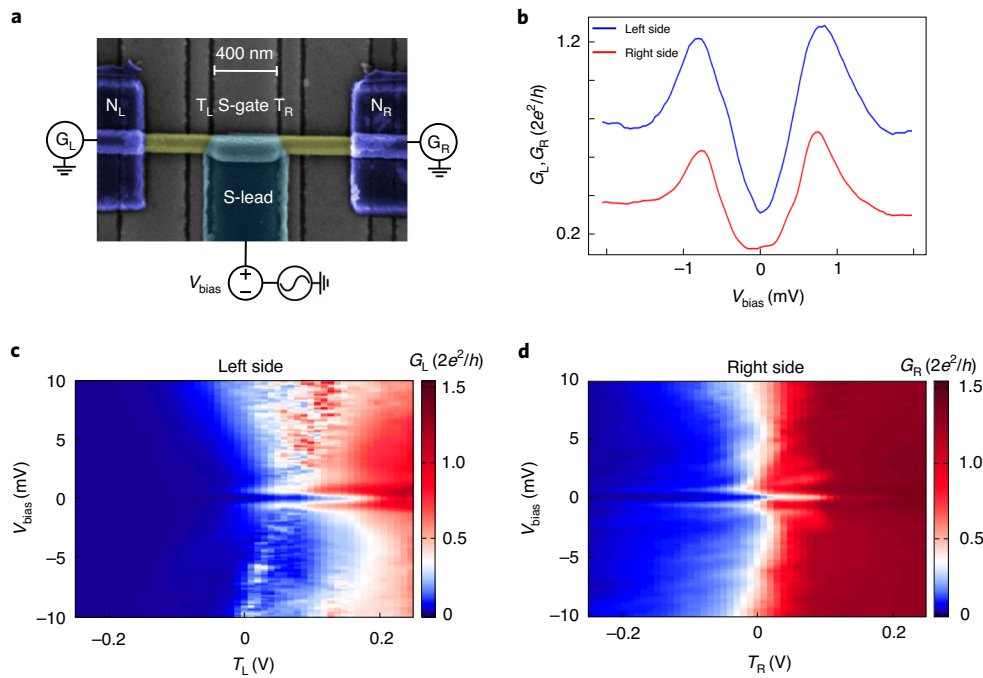


**Fig. 1 | Three-terminal nanowire device and basic characterizations.** **a**, False-colour scanning electron micrograph of the measured device and the circuit diagram. **b**, Induced gap from both sides in the pinch off regime, with tunnel-gate voltages of  $-0.015$  V ( $T_L$ ) and  $-0.075$  V ( $T_R$ ) and S-gate voltage of  $-0.75$  V. **c,d**, Differential conductance  $G_L$  (**c**) and  $G_R$  (**d**) as functions of tunnel-gate voltages and source-drain voltage. All the other gates are set to positive voltages (open regime) and the magnetic field is set to  $B=0$ .

$G_L$  and  $G_R$  are measured at the two normal contacts with a standard lock-in technique. Fabrication and measurement details are described further in the Methods.

To characterize the tunnel barriers and induce superconductivity, we first performed measurements at zero magnetic field. Figure 1b shows the results of low-voltage-bias spectroscopy for  $G_L$  and  $G_R$  measured at the same setting of the S-gate. By setting either the left or the right tunnel gate to the pinch off regime we observe soft and smoothly induced superconducting gaps of  $760\text{--}800$   $\mu\text{eV}$ , typical for partially covered NbTiN/InSb devices. The gap is defined by two finite-bias quasiparticle peaks with no sharp resonances in between.

Figures 1c,d presents the characterization of the tunnel barriers over a large range of voltage bias values exceeding the induced gap, and the conductance varies from a few percent of  $2e^2/h$  to above the conductance quantum. Both on the left and the right side, conductances evolve largely monotonically, revealing no randomly formed quantum dots. The induced gap features persist over a wide range of conductance. A limited range of tunnel-gate voltage  $T_L$  triggers charge instabilities that manifest as rapid conductance switches. In what follows, we set the tunnel barriers to attain similar total conductance on the left and right, trying to avoid the unstable regimes.

Figure 2 presents zero-bias conductance peaks measured on the left side. Near zero magnetic field,  $G_L$  exhibits a soft gap without resonances at low bias, as illustrated in Fig. 1. At  $B > 0.3$  T, conductance resonances are observed near zero bias: they are either a ZBCP or a split peak around zero bias. The peak conductance increases as the magnetic field increases, and reaches a value of  $2e^2/h$  near  $B = 1.0$  T, while the conductance beyond the gap remains nearly unchanged (Fig. 2b). In Fig. 2c, bias voltage linecuts at 0 T and 1 T show the shape of the gap and the ZBCP. The ZBCP in Fig. 2c has a full-width at half-maximum of  $150$   $\mu\text{eV}$  and reaches a conductance of nearly  $2e^2/h$ . The peak prominence above the background is of order  $0.4 \times e^2/h$ . Without correcting for any unknown contact resistances

in the device, we find a peak value of  $0.8 \times e^2/h$ , and to achieve exact quantization, we have to correct for a series resistance of  $4$  k $\Omega$ , a value that could be attributed to the two interface resistances. The issue of unknown contact resistance is generic to all experiments where the exact quantization is not independently established (an extended discussion is provided in the Methods and Extended Data Figs. 1 and 2).

To study the behaviour of this ZBCP in relation to barrier transmission, we set the magnetic field to 1 T and varied the voltage on tunnel gate  $T_L$  (Fig. 2d). The ZBCP only appears above  $T_L = -0.07$  V and is stable for a finite range of  $T_L$ . When the ZBCP first appears, it immediately reaches its peak conductance of nearly  $2e^2/h$ , and maintains this conductance for a small range of  $T_L$  until the ZBCP conductance increases above the quantized value predicted for Majorana modes (Fig. 2e). The Majorana conductance may exceed  $2e^2/h$  only if the barrier has multiple transmitting channels<sup>10</sup>, and indeed, here, the above-gap conductance reaches beyond  $2e^2/h$  for more positive  $T_L$ .

Another check for the Majorana origins of a ZBCP is in its behaviour as a function of magnetic field angle with respect to the nanowire. Majorana states are predicted to appear only when the applied field is orthogonal to the effective spin-orbit field, previously measured to be perpendicular to the nanowire<sup>28,29</sup>. Note that this measurement can be performed in NbTiN due to the large critical field, but it is not practical in devices with thin Al shells because of the very small out-of-plane critical field. As shown in Fig. 2f, the ZBCP on the left side reaches  $2e^2/h$  when the magnetic field is parallel to the nanowire and perpendicular to the spin-orbit field. Notably, a deviation of a few degrees results in the splitting of the ZBCP and a drop in conductance. More magnetic field anisotropy data are provided in Extended Data Fig. 3.

Overall, the behaviour of the ZBCP, as it is presented in Fig. 2, is consistent with Majorana theory, which dictates that the Majorana ZBCP should emerge at finite magnetic field applied

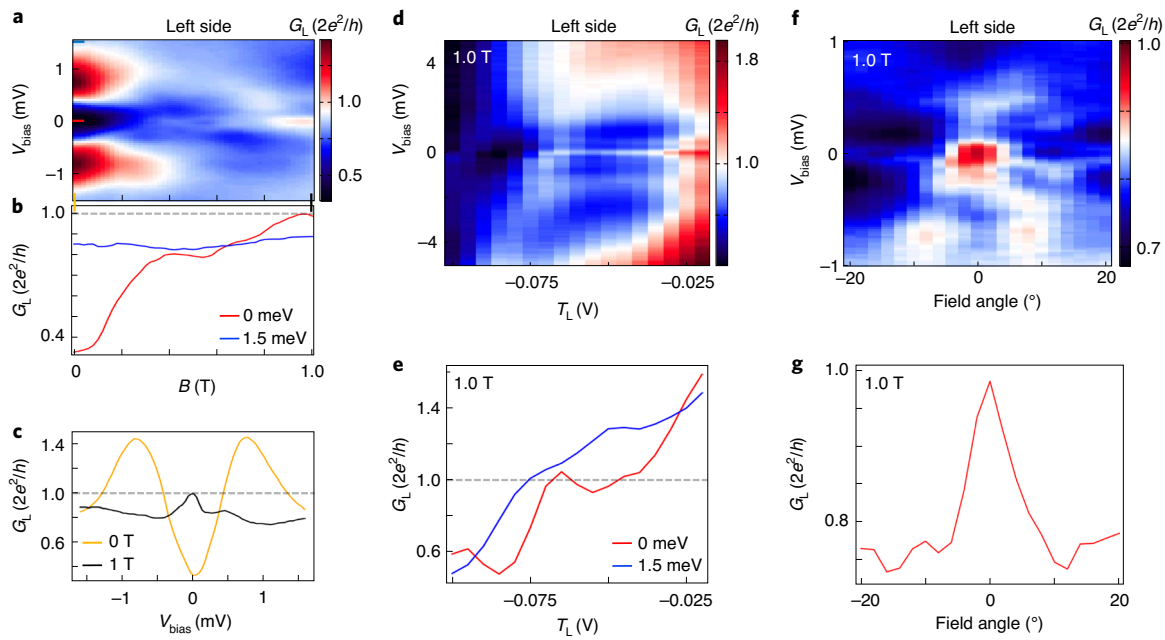


**Fig. 2 | Nearly quantized ZBCP on the left side.** **a**, Magnetic field dependence for S-gate =  $-0.17$  V,  $T_L = -0.045$  V and  $T_R = -0.105$  V. The field direction is parallel to the nanowire. **b**, Linecuts taken at  $V_{\text{bias}} = 0$  and  $1.5$  meV from **a**. **c**, Bias voltage linecuts from **a** at  $0$  T and at  $1$  T show the shape of the gap and the nearly quantized ZBCP. **d**, Tunnel-gate  $T_L$  dependence of the ZBCP. **e**, Linecuts taken at  $V_{\text{bias}} = 0$  and  $1.5$  meV from **d**. A conductance plateau of nearly  $2e^2/h$  associated with the ZBCP appear at zero bias, while the conductance above the gap evolve monotonically. **f**, Field angle dependence of the ZBCP at  $1$  T.  $0^\circ$  means the field is parallel to the nanowire and perpendicular to the spin-orbit field. **g**, Linecut at zero bias from **f**, showing a small deviation from the  $0^\circ$  results in the drop of conductance from the quantized value. Note that a contact resistance of  $4$  k $\Omega$  is subtracted.

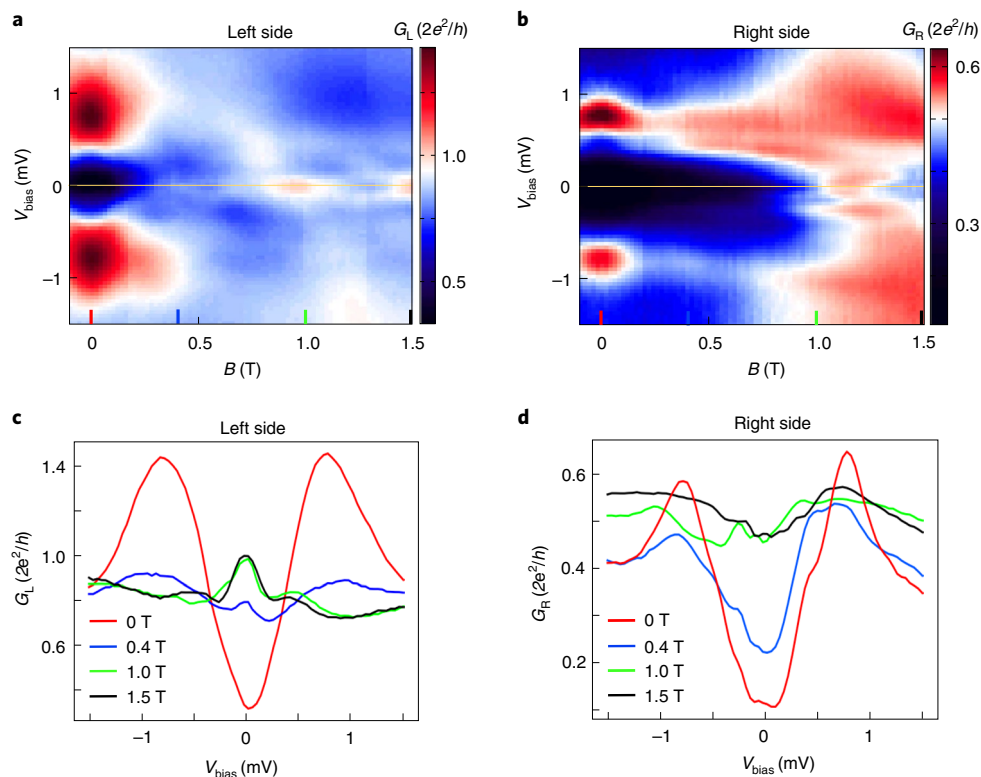


**Fig. 3 | Absence of zero-bias peak on the right side.** **a, b**, Magnetic field dependence of the subgap states on the left (**a**) and right (**b**) sides from the same dataset as in Fig. 2a, now in an expanded field range, with an S-gate voltage of  $-0.17$  V,  $T_L = -0.045$  V and  $T_R = -0.105$  V. A contact resistance of  $4$  k $\Omega$  is subtracted for the left side. **c, d**, Bias linecuts at  $0$  T,  $0.4$  T,  $1.0$  T and  $1.5$  T taken from **a** (**c**) and **b** (**d**).

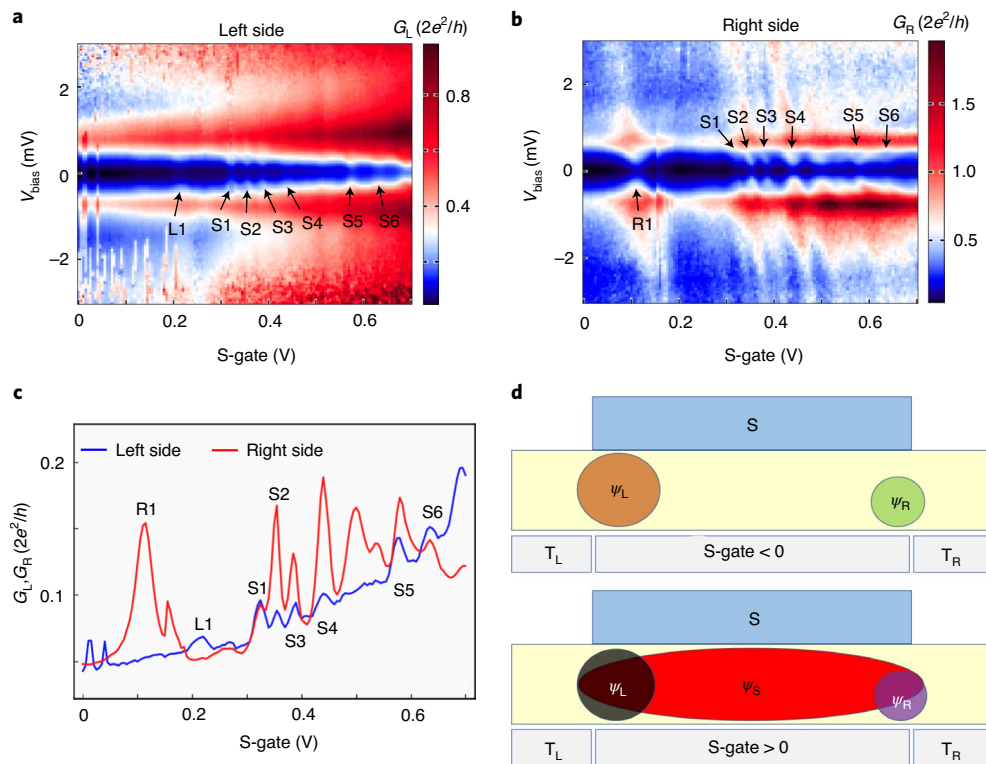


**Fig. 4 | Localized and delocalized states.** **a, b**, Differential conductance  $G_L$  (**a**) and  $G_R$  (**b**) as functions of source–drain voltage and S-gate voltage, showing localized and delocalized states at zero magnetic field. Tunnel-gate voltages  $T_L$  and  $T_R$  are set to  $-0.175$  V and  $0.09$  V, respectively. **c**, Linecuts at zero bias taken from **a** and **b** showing the overlapping delocalized states and distinct localized states. **d**, Sketches of the wavefunction configuration in the device for negative and positive S-gate voltages.

along the nanowire, persist in the magnetic field, reach a peak height of  $2e^2/h$  and be independent of the tunnel barrier strength.

However, the simultaneous examination of conductance on both sides of the device reveals a major deviation from the basic Majorana picture: no ZBCP is observed on the right side to accompany the left-side ZBCP from Fig. 2. Figure 3a originates from the same dataset as Fig. 2a, but now we reveal a larger magnetic field range. Apart from the nearly quantized ZBCP described in Fig. 2, another peak splitting is observed at 1.2 T followed by another region of a  $2e^2/h$  ZBCP around 1.5 T. Figure 3b shows the simultaneously acquired conductance from the right side. Although subgap resonances are also observed at finite fields, there is no quantized ZBCP; in fact, no ZBCP of any height is observed on the right side in this regime upon scanning S-gate and  $T_R$  (more information is provided in Extended Data Figs. 4–6). Linecuts taken from Fig. 3a,b show that the left side has high-conductance ZBCPs at 0.4 T, 1.0 T and 1.5 T, while the right side does not have ZBCPs at those magnetic fields.

Next, we discuss the possible interpretations of ZBCPs observed only on the left side of the device. A ZBCP in nanowire devices is known to have many other origins not related to Majorana modes. In particular, trivial Andreev bound states in quantum dots have been shown to exhibit ZBCP and some degree of resonance pinning to zero bias due to gap closing and level repulsion from higher energy states<sup>23,26,30–34</sup>. Disorder-induced ZBCPs can appear due to spectral crowding near zero bias. Finally, fine-tuned so-called ‘class D’ peaks can manifest in the intermediate mesoscopic regime, which does not correspond to a large disordered ensemble of states<sup>35–39</sup>; this is a concept closely related to a set of a few randomly coupled quantum dots<sup>32,40</sup>. There is no fundamental reason why any of such non-Majorana ZBCPs could not be tuned to have peak conductance close to a particular value, including the quantized value.

On the other hand, is it still possible that the left-side ZBCP is due to a Majorana mode? In such a scenario, the second Majorana bound state should be somewhere to the right of the left Majorana bound state. Within the relatively short S-lead segment of the nanowire, which is 400 nm in length, while the nanowire itself has a diameter of 120 nm, there is little room to locate the right Majorana. After all, it cannot be on the right edge of the S contact where no ZBCP is observed. It is unlikely that a possible left and right Majorana have no overlap, as both need to fit in a wire section only approximately two wire diameters long. Majorana overlap generically induces peak splitting. Thus, interpreting the observed ZBCP as Majorana hinges on a multitude of assumptions, each of which has to play out favourably in just the right way.

Next we address whether any wavefunction can be confirmed as delocalized between the left and right tunnel barriers. This is important for demonstrating how wavefunction localization can be explored in the three-terminal geometry. It is also important for assessing the potential of nanowire devices in future Majorana experiments because Majoranas are expected to be generated from delocalized subgap states.

In Figs. 1–3, we study subgap resonances at finite magnetic field while the S-gate is set to negative voltages, that is, closer to the few-subband regime that is interesting for Majorana modes. In that regime, we do not clearly observe delocalized states. To find delocalized states, we ramp the magnetic field to zero and shift to positive voltage on the S-gate, that is, into the higher-density regime (Fig. 4a,b). We observe resonances that exist both above the gap as well as within the soft gap, suggesting that they are not generated by Andreev reflections. They may be a manifestation of higher-momentum wavefunctions that are localized away from the semiconductor–superconductor interface and closer to the bottom

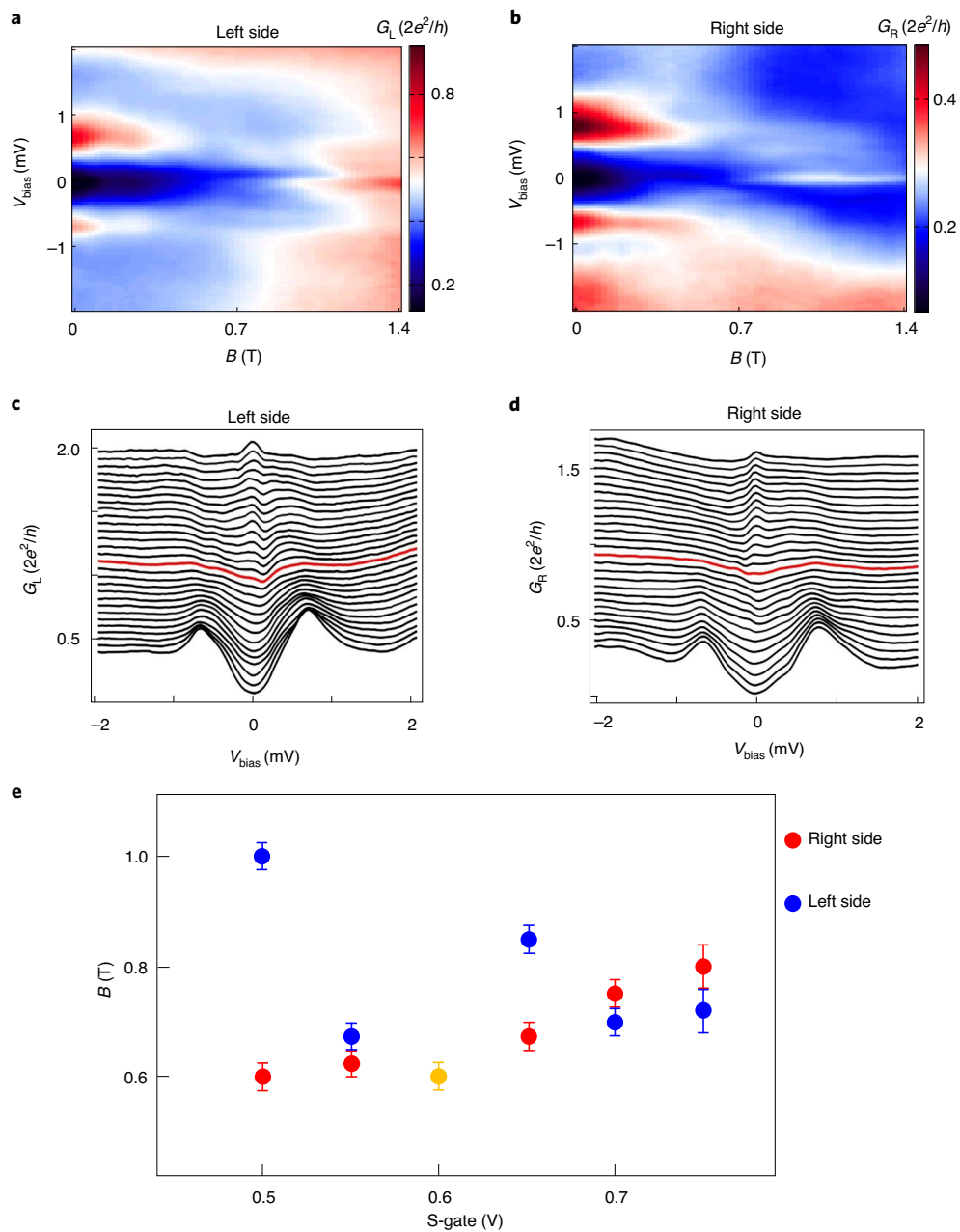


**Fig. 5 | Accidentally correlated ZBCPs from both sides.** **a, b**, Magnetic field dependences of  $G_L$  (**a**) and  $G_R$  (**b**) with an S-gate voltage of 0.6 V and  $T_L = -0.15$  V and  $T_R = 0.09$  V. **c, d**, Bias linecuts taken from **a** (**c**) and **b** (**d**) with an interval field of 0.05 T. The onset field of ZBCP (0.6 T) is highlighted in red. **e**, The onset magnetic fields of ZBCP for the left and right sides extracted from Extended Data Fig. 9. The orange circle corresponds to data in **a-d**. The error bars are determined by the field scan resolution.

of the nanowire. Such resonances were previously observed in similar devices<sup>11</sup>.

Even in the positive S-gate regime we still observe resonances that are unique to either the left or the right side. We label such resonances with ‘L’ or ‘R’. For example, when the S-gate is close to 0.11 V, there is a visible resonance on the right side, which we label ‘R1’. On the left side, however, there is no such resonance around the same S-gate voltage. Instead, there is a resonance at S-gate = 0.22 V, which we label ‘L1’. Resonances that are observed in both  $G_L$  and  $G_R$  simultaneously are labelled ‘S’-resonances: for example six delocalized resonances S1–S6 are labelled in Fig. 4a–c. Figure 4d provides a schematic summary of the findings of zero-field three-terminal measurements. For negative S-gate voltages, two independent sets of bound

states are observed on the left and the right side. For more positive S-gate voltages, some delocalized states are observed while the localized states are still present. The delocalized states only appear at low field, and there is no regime with only delocalized states in this device. Even when the voltage on the S-gate is above 0.5 V, localized states still exist. (More data are provided in Extended Data Figs. 7 and 8 and in a separate forthcoming manuscript.) We note that similar findings were reached by studying NbTiN/InSb devices with multiple S-gates in the two-terminal geometry: for more positive settings of the S-gate nearest to the tunnel gate, states sensitive to the far-away S-gates were observed<sup>11</sup> (Supplementary Information).

Although the three-terminal geometry can be a powerful method of diagnosing the localization of wavefunctions, it is not immune to

fine-tuning, which can create the appearance of correlated ZBCPs (Fig. 5). For a specific setting of the S-gate at 0.6 V, which is between two delocalized resonances as shown in Extended Data Fig. 8, we observe zero-bias conductance peaks with onset at  $B = 0.6$  T in both  $G_L$  and  $G_R$  and that persist to over 1.4 T. Even though these peaks are not near the quantized conductance value, such correlation can be used to suggest that Majorana modes are observed. However, the correlation is not robust and vanishes when the S-gate is varied, as shown in Fig. 5e, which plots the onset fields of ZBCPs on the left and right sides as the S-gate voltage is varied (full data are provided in Extended Data Fig. 9). Generically, zero-bias or near-zero-bias resonances exhibit no verifiable correlations between  $G_L$  and  $G_R$  in this device.

We emphasize that the length of the superconducting island explored in this work is 400 nm, which is shorter than in many of the previous Majorana-motivated experiments. Because localized wavefunctions resulting in nearly quantized ZBCPs can be observed for 400-nm-long islands, there is little practical utility in exploring longer islands, for example 600 nm, while maintaining the same overall device fabrication method. Exploring shorter superconductors, such as 200-nm-long islands, is likely to enhance the frequency of observing correlated subgap states in  $G_L$  and  $G_R$ . However, at such a short length it will be difficult to argue a delocalized Majorana as the origin of the correlated signal. To summarize, the three-terminal geometry offers a way to identify non-Majorana states even if local two-terminal measurements are consistent with Majorana zero modes. The key lesson is that individual Majorana signatures may originate from trivial states and be a result of fine-tuning or data selection performed to match a theory expectation. We believe a way to reliably identify Majorana modes is to simultaneously observe many Majorana signatures in a single device. This would reduce the role of fine-tuning and diminish the likelihood of an alternative explanation. Although correlated ZBCPs in the three-terminal geometry alone do not uniquely identify Majorana zero modes, future improvements in growth and fabrication can open the possibility of observing delocalized Majorana wavefunctions in the three-terminal geometry when accompanied by other phenomena predicted to be associated with Majorana zero modes.

### Online content

Any methods, additional references, Nature Research reporting summaries, source data, extended data, supplementary information, acknowledgements, peer review information; details of author contributions and competing interests; and statements of data and code availability are available at <https://doi.org/10.1038/s41567-020-01107-w>.

Received: 13 May 2020; Accepted: 28 October 2020;

Published online: 04 January 2021

### References

- Oreg, Y., Refael, G. & von Oppen, F. Helical liquids and Majorana bound states in quantum wires. *Phys. Rev. Lett.* **105**, 177002 (2010).
- Lutchyn, R. M., Sau, J. D. & Das Sarma, S. Majorana fermions and a topological phase transition in semiconductor–superconductor heterostructures. *Phys. Rev. Lett.* **105**, 077001 (2010).
- Mourik, V. et al. Signatures of Majorana fermions in hybrid superconductor–semiconductor nanowire devices. *Science* **336**, 1003–1007 (2012).
- Albrecht, S. M. et al. Exponential protection of zero modes in Majorana islands. *Nature* **531**, 206–209 (2016).
- Deng, M. T. et al. Majorana bound state in a coupled quantum-dot hybrid-nanowire system. *Science* **354**, 1557–1562 (2016).
- Frolov, S., Manfra, M. & Sau, J. Topological superconductivity in hybrid devices. *Nat. Phys.* **16**, 718–724 (2020).
- Sengupta, K., Žutić, I., Kwon, H.-J., Yakovenko, V. M. & Das Sarma, S. Midgap edge states and pairing symmetry of quasi-one-dimensional organic superconductors. *Phys. Rev. B* **63**, 144531 (2001).
- Law, K. T., Lee, P. A. & Ng, T. K. Majorana fermion induced resonant Andreev reflection. *Phys. Rev. Lett.* **103**, 237001 (2009).
- Flensberg, K. Tunneling characteristics of a chain of Majorana bound states. *Phys. Rev. B* **82**, 180516 (2010).
- Wimmer, M., Akhmerov, A. R., Dahlhaus, J. P. & Beenakker, C. W. J. Quantum point contact as a probe of a topological superconductor. *New J. Phys.* **13**, 053016 (2011).
- Nichele, F. et al. Scaling of Majorana zero-bias conductance peaks. *Phys. Rev. Lett.* **119**, 136803 (2017).
- Klitzing, K. V., Dorda, G. & Pepper, M. New method for high-accuracy determination of the fine-structure constant based on quantized Hall resistance. *Phys. Rev. Lett.* **45**, 494–497 (1980).
- van Wees, B. J. et al. Quantized conductance of point contacts in a two-dimensional electron gas. *Phys. Rev. Lett.* **60**, 848–850 (1988).
- van Houten, H. & Beenakker, C. W. J. Quantum point contacts. *Phys. Today* **49**, 22 (1996).
- Klinovaja, J., Schmidt, M. J., Braunecker, B. & Loss, D. Helical modes in carbon nanotubes generated by strong electric fields. *Phys. Rev. Lett.* **106**, 156809 (2011).
- Quay, C. et al. Observation of a one-dimensional spin–orbit gap in a quantum wire. *Nat. Phys.* **6**, 336–339 (2010).
- Nowack, K. C. et al. Imaging currents in HgTe quantum wells in the quantum spin Hall regime. *Nat. Mater.* **12**, 787–791 (2013).
- König, M. et al. Quantum spin Hall insulator state in HgTe quantum wells. *Science* **318**, 766–770 (2007).
- Read, N. & Green, D. Paired states of fermions in two dimensions with breaking of parity and time-reversal symmetries and the fractional quantum Hall effect. *Phys. Rev. B* **61**, 10267–10297 (2000).
- Moore, G. & Read, N. Nonabelions in the fractional quantum Hall effect. *Nucl. Phys. B* **360**, 362–396 (1991).
- Nayak, C., Simon, S. H., Stern, A., Freedman, M. & Das Sarma, S. Non-Abelian anyons and topological quantum computation. *Rev. Mod. Phys.* **80**, 1083–1159 (2008).
- Pientka, F., Kells, G., Romito, A., Brouwer, P. W. & von Oppen, F. Enhanced zero-bias Majorana peak in the differential tunneling conductance of disordered multisubband quantum-wire/superconductor junctions. *Phys. Rev. Lett.* **109**, 227006 (2012).
- Prada, E., San-Jose, P. & Aguado, R. Transport spectroscopy of ns nanowire junctions with Majorana fermions. *Phys. Rev. B* **86**, 180503 (2012).
- Lin, C.-H., Sau, J. D. & Das Sarma, S. Zero-bias conductance peak in Majorana wires made of semiconductor/superconductor hybrid structures. *Phys. Rev. B* **86**, 224511 (2012).
- Rainis, D., Trifunovic, L., Klinovaja, J. & Loss, D. Towards a realistic transport modeling in a superconducting nanowire with Majorana fermions. *Phys. Rev. B* **87**, 024515 (2013).
- Liu, C.-X., Sau, J. D. & Das Sarma, S. Role of dissipation in realistic Majorana nanowires. *Phys. Rev. B* **95**, 054502 (2017).
- Pan, H., Cole, W. S., Sau, J. D. & Das Sarma, S. Generic quantized zero-bias conductance peaks in superconductor–semiconductor hybrid structures. *Phys. Rev. B* **101**, 024506 (2020).
- Nadj-Perge, S. et al. Spectroscopy of spin–orbit quantum bits in indium antimonide nanowires. *Phys. Rev. Lett.* **108**, 166801 (2012).
- Středa, P. & Šeba, P. Antisymmetric spin filtering in one-dimensional electron systems with uniform spin–orbit coupling. *Phys. Rev. Lett.* **90**, 256601 (2003).
- Lee, E. J. et al. Spin-resolved Andreev levels and parity crossings in hybrid superconductor–semiconductor nanostructures. *Nat. Nanotechnol.* **9**, 79–84 (2014).
- Kells, G., Meidan, D. & Brouwer, P. W. Near-zero-energy end states in topologically trivial spin–orbit coupled superconducting nanowires with a smooth confinement. *Phys. Rev. B* **86**, 100503 (2012).
- Woods, B. D., Chen, J., Frolov, S. M. & Stanescu, T. D. Zero-energy pinning of topologically trivial bound states in multiband semiconductor–superconductor nanowires. *Phys. Rev. B* **100**, 125407 (2019).
- Vuik, A., Nijholt, B., Akhmerov, A. R. & Wimmer, M. Reproducing topological properties with quasi-Majorana states. *SciPost Phys.* **7**, 061 (2019).
- Moore, C., Zeng, C., Stanescu, T. D. & Tewari, S. Quantized zero-bias conductance plateau in semiconductor–superconductor heterostructures without topological Majorana zero modes. *Phys. Rev. B* **98**, 155314 (2018).
- Motrunich, O., Damle, K. & Huse, D. A. Griffiths effects and quantum critical points in dirty superconductors without spin–rotation invariance: one-dimensional examples. *Phys. Rev. B* **63**, 224204 (2001).
- Brouwer, P. W., Duckheim, M., Romito, A. & von Oppen, F. Topological superconducting phases in disordered quantum wires with strong spin–orbit coupling. *Phys. Rev. B* **84**, 144526 (2011).
- Brouwer, P. W., Duckheim, M., Romito, A. & von Oppen, F. Probability distribution of Majorana end-state energies in disordered wires. *Phys. Rev. Lett.* **107**, 196804 (2011).

38. Sau, J. D. & Das Sarma, S. Density of states of disordered topological superconductor–semiconductor hybrid nanowires. *Phys. Rev. B* **88**, 064506 (2013).
39. Pikulin, D. I., Dahlhaus, J. P., Wimmer, M., Schomerus, H. & Beenakker, C. W. J. A zero-voltage conductance peak from weak antilocalization in a Majorana nanowire. *New J. Phys.* **14**, 125011 (2012).
40. Chen, J. et al. Ubiquitous non-Majorana zero-bias conductance peaks in nanowire devices. *Phys. Rev. Lett.* **123**, 107703 (2019).
41. Chen, J. et al. Experimental phase diagram of zero-bias conductance peaks in superconductor/semiconductor nanowire devices. *Sci. Adv.* **3**, e1701476 (2017).

**Publisher's note** Springer Nature remains neutral with regard to jurisdictional claims in published maps and institutional affiliations.

© The Author(s), under exclusive licence to Springer Nature Limited 2021

## Methods

**Nanowire growth, wire deposition and contact deposition.** The InSb nanowires were grown in a metal–organic vapour-phase epitaxy reactor using a Au catalyst. A typical nanowire was 3–5- $\mu\text{m}$  long with a diameter of 120–150 nm. The InSb nanowires were transferred under an optical microscope: a fine needle attached to a micromanipulator was used to pick up nanowires from the mother chip and deposit them onto the desired fine gates with submicrometre accuracy. After the nanowire transfer, contact patterns were written on PMMA 950A4 resist using electron-beam lithography, then 5-nm NbTi and 60-nm NbTiN were sputtered onto the nanowire with an angle of  $60^\circ$  in relation to the chip substrate. In a separate lithography cycle, 10-nm Ti and 100-nm Pd were evaporated onto the chip as normal contacts. Before each metal deposition we used a standard sulfur passivation process to remove the native oxide on the nanowire, followed by a 10-s low-power in situ argon sputter cleaning.

**Measurements.** Measurements were performed in a dilution refrigerator at a base temperature of 40 mK. Two lock-in amplifiers were used to measure the two sides of the device simultaneously using the standard low-frequency lock-in technique (77.77 Hz, 5  $\mu\text{V}$ ). Multiple stages of filtering were used to enhance the signal-to-noise ratio. For all the measurements, a bias voltage was applied to the superconducting contact and the two normal contacts were grounded. We normalized the differential conductance directly measured with the two lock-in amplifiers, as described in the next section.

**Conductance normalization procedure.** To obtain the actual differential conductance  $dI/dV$  on both sides, we must correct the measured differential conductance from the lock-in, removing the contribution from the measurement circuit. First, we need to subtract the series resistances of the wiring, the RC filters and the input impedance of the amplifier. As indicated in Extended Data Fig. 1b, the a.c. lock-in voltage  $\Delta V_{ac}$  will drop across  $R_{wire}$  and  $R_{filters}$  of the voltage bias line. This voltage drop is  $\Delta V_s = (\Delta I_L + \Delta I_R)(R_{wire} + R_{filters})$ , where  $\Delta I_L$  and  $\Delta I_R$  are the a.c. current passing through the left side and the right side of the device, respectively. For the left side, the a.c. voltage drops across the second set of RC filters of the normal contact line, the d.c. wires and the impedance of the amplifier. This voltage drop is given by  $\Delta V_n = \Delta I_L(R_{wire} + R_{filters} + R_{im})$ . The a.c. voltage applied to the nanowire device on the left side is then  $\Delta V_L = \Delta V_{ac} - \Delta V_s - \Delta V_n$  and the corrected  $G'_L$  for the left side is

$$G'_L = \frac{dI_L}{dV_L} = \frac{dI_L}{dV_{ac}} \frac{dV_{ac}}{dV_L} = G_L \left( \frac{1}{1 - \frac{\Delta V_s}{\Delta V_{ac}} - \frac{\Delta V_n}{\Delta V_{ac}}} \right) = G_L \left( \frac{1}{1 - (G_L + G_R)(R_{wire} + R_{filters}) - G_L(R_{wire} + R_{filters} + R_{im})} \right)$$

$G_L = \frac{dI_L}{dV_{ac}}$  and  $G_R = \frac{dI_R}{dV_{ac}}$  are the measured differential conductances from the lock-ins connected to the left side and the right side respectively. Similarly:

$$G'_R = G_R \left( \frac{1}{1 - (G_L + G_R)(R_{wire} + R_{filters}) - G_R(R_{wire} + R_{filters} + R_{im})} \right)$$

In the main text and Extended Data, ' $G_L$ ' and ' $G_R$ ' represent corrected differential conductances (which may also include subtraction of contact resistance if indicated) for the left side and right side, respectively.

A unique difficulty in unambiguously establishing quantized Majorana conductance is methodological in nature. Quantized Majorana conductance is predicted to occur even when the tunnel barrier transmission is non-monotonic and does not exhibit quantized conductance plateaux<sup>10</sup>. However, under realistic conditions in nanowire devices featuring some degree of disorder, it is more likely that only a single quantized Majorana appears, but no higher quantized plateaux. As a consequence, the absolute value of conductance cannot be calibrated accurately, as only a single value of known conductance (that is the presumed quantized Majorana conductance) is present, which needs to be corrected for series resistances inevitably present in the measurement circuitry and the device. The series resistances caused by metal–semiconductor interfaces can only be roughly estimated, but not measured independently. This methodological challenge prevents accurately verifying the exact conductance at a supposed quantized plateau due to a Majorana.

In the present work, we do consider the influence of the contact resistance. In Figs. 2 and 3 and Extended Data Fig. 10,  $R_L = 4 \text{ k}\Omega$  was subtracted to fit the ZBCP to  $2e^2/h$ . This contact resistance value is also consistent with the saturation resistance determined in Extended Data Fig. 2a. It is easy to decide the contact resistance in experiments such as quantum point contact measurements, because it is possible to fit the conductance plateau sequence to the anticipated quantized values. However, in our experiment, the actual  $R_L$  is hard to determine, given the fact that we do not see a well-defined conductance plateau from subband-resolved transport and the origin of the ZBCP is unlikely due to Majorana. Series resistance can be extracted from the saturation conductance at positive gate voltages, but this method is also prone to inaccuracy due to gate screening and other factors. In Extended Data Fig. 1e, we present a series of linecuts with different  $R_L$  subtracted

from the same dataset of Fig. 2d. As we can see, with  $R_L$  increased from 0 to 5 k $\Omega$ , the height of the plateau has grown from  $0.8 \times 2e^2/h$  to around  $1.1 \times 2e^2/h$ .

**Further reading.** Background information on Majorana modes in nanowires and topological quantum computing is provided in refs. 42,43. For nanowire growth, details can be found in ref. 44. These are some of the previous experiments reporting Majorana modes in nanowires<sup>3,45–48</sup> and Majorana non-locality<sup>4,49</sup>. Other three-terminal measurement works are reported in refs. 50–52. For theory about conductance quantization without Majorana modes, see refs. 27,34.

**Volume and duration of study.** To study the delocalized states and quantized ZBCP, 15 chips were fabricated and cooled down, and 41 three-terminal devices were measured on them. About half of the devices had high contact resistance and were not studied in detail. Nineteen devices were studied in detail, among which four devices showed delocalized states. Two devices showed ZBCPs with conductance close to  $2e^2/h$ , although high-conductance ZBCPs were not the focus of all cooldowns. For the device studied in this Letter,  $\sim 7,000$  useful datasets were obtained within three months.

## Data availability

An extended curated data ontology including all data within this paper and data on other three-terminal devices is provided on Zenodo (<https://doi.org/10.5281/zenodo.3958243>). An interactive Jupyter notebook containing data in this paper is on GitHub (<https://mybinder.org/v2/gh/frolovgroup/Quantized-Zero-Bias-Peaks-from-trivial-states-in-Majorana-nanowire-devices/329582d89729de51f7b0177d2774bd1bc3e75e53>).

## References

- Lutchyn, R. M. et al. Majorana zero modes in superconductor–semiconductor heterostructures. *Nat. Rev. Mater.* **3**, 52–68 (2018).
- Stern, A. & Lindner, N. H. Topological quantum computation—from basic concepts to first experiments. *Science* **339**, 1179–1184 (2013).
- Badawy, G. et al. High mobility stemless InSb nanowires. *Nano Lett.* **19**, 3575–3582 (2019).
- Rokhinson, L. P., Liu, X. & Furdyna, J. K. The fractional a.c. Josephson effect in a semiconductor–superconductor nanowire as a signature of Majorana particles. *Nat. Phys.* **8**, 795–799 (2012).
- Deng, M. T. et al. Anomalous zero-bias conductance peak in a Nb–InSb nanowire–Nb hybrid device. *Nano Lett.* **12**, 6414–6419 (2012).
- Das, A. et al. Zero-bias peaks and splitting in an Al–InAs nanowire topological superconductor as a signature of Majorana fermions. *Nat. Phys.* **8**, 887–895 (2012).
- Churchill, H. O. H. et al. Superconductor–nanowire devices from tunneling to the multichannel regime: zero-bias oscillations and magnetoconductance crossover. *Phys. Rev. B* **87**, 241401 (2013).
- Deng, M.-T. et al. Nonlocality of Majorana modes in hybrid nanowires. *Phys. Rev. B* **98**, 085125 (2018).
- Anselmetti, G. L. R. et al. End-to-end correlated subgap states in hybrid nanowires. *Phys. Rev. B* **100**, 205412 (2019).
- Gramich, J., Baumgartner, A. & Schönenberger, C. Andreev bound states probed in three-terminal quantum dots. *Phys. Rev. B* **96**, 195418 (2017).
- Cohen, Y. et al. Nonlocal supercurrent of quartets in a three-terminal Josephson junction. *Proc. Natl Acad. Sci. USA* **115**, 6991–6994 (2018).

## Acknowledgements

We thank S. Gazibegovic for assistance with growing nanowires. This work was supported by NSF PIRE-1743717, NSF DMR-1906325, ONR and ARO.

## Author contributions

G.B. and E.P.A.M.B. provided the nanowires. P.Y. and J.C. fabricated the devices. P.Y. and M.G. performed the measurements. P.Y., K.Z., V.M. and S.M.F. analysed the results and wrote the manuscript, with contributions from all of the authors.

## Competing interests

The authors declare no competing interests.

## Additional information

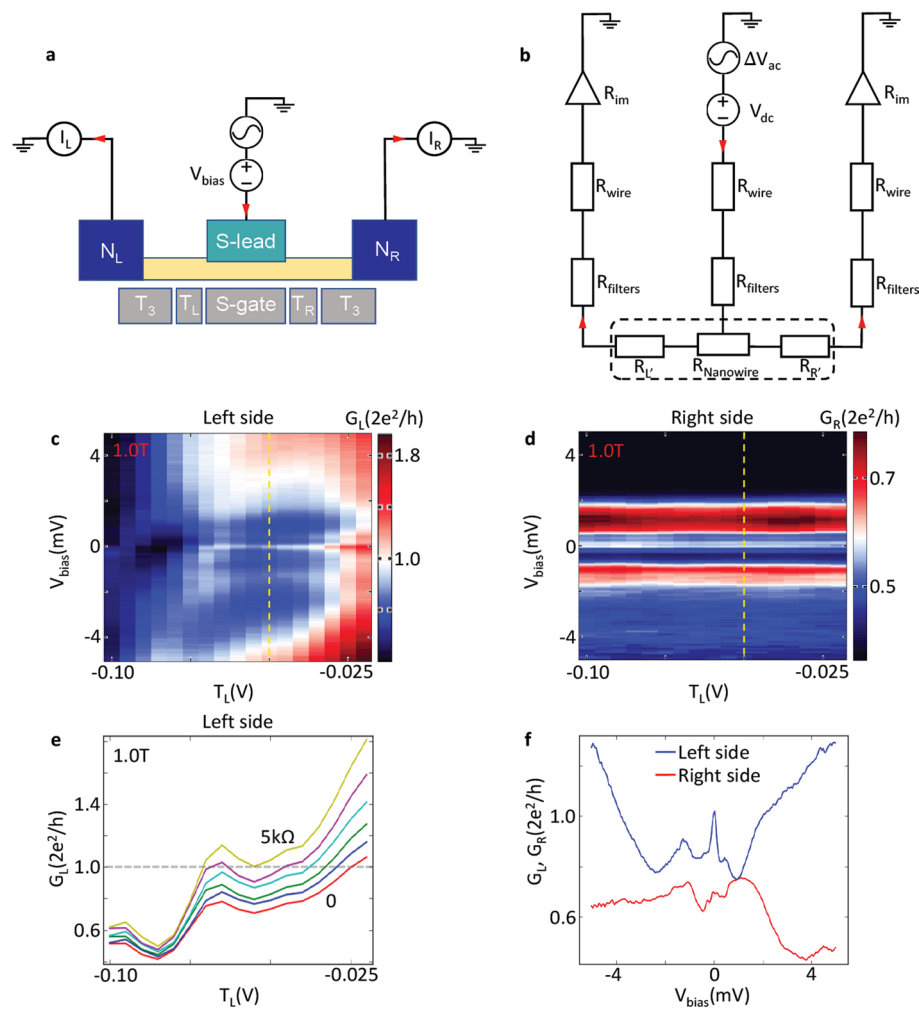
**Extended data** is available for this paper at <https://doi.org/10.1038/s41567-020-01107-w>.

**Supplementary information** is available for this paper at <https://doi.org/10.1038/s41567-020-01107-w>.

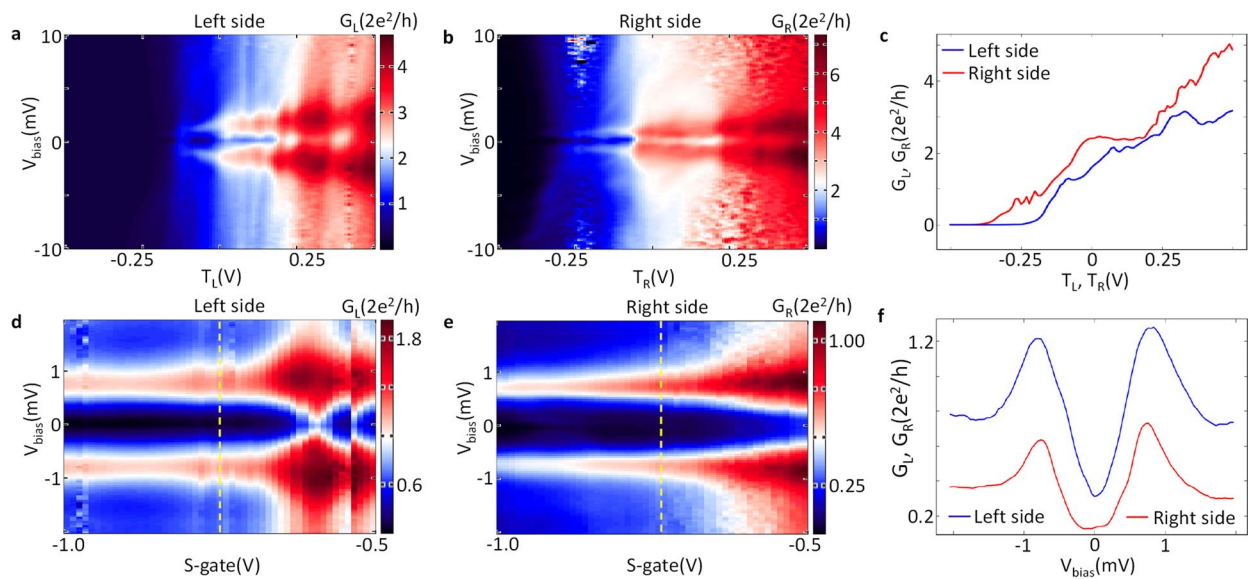
**Correspondence and requests for materials** should be addressed to S.M.F.

**Peer review information** *Nature Physics* thanks the anonymous reviewers for their contribution to the peer review of this work.

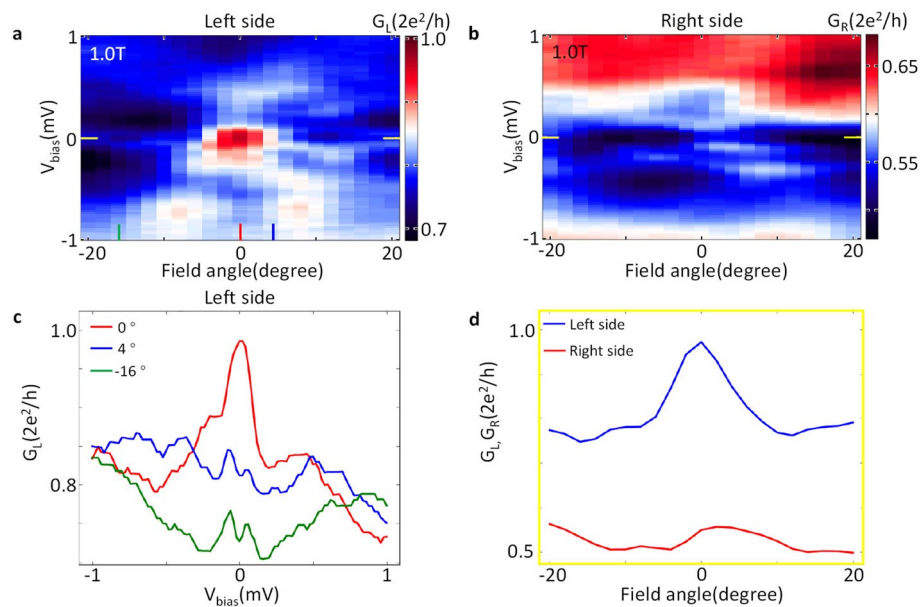
**Reprints and permissions information** is available at [www.nature.com/reprints](http://www.nature.com/reprints).



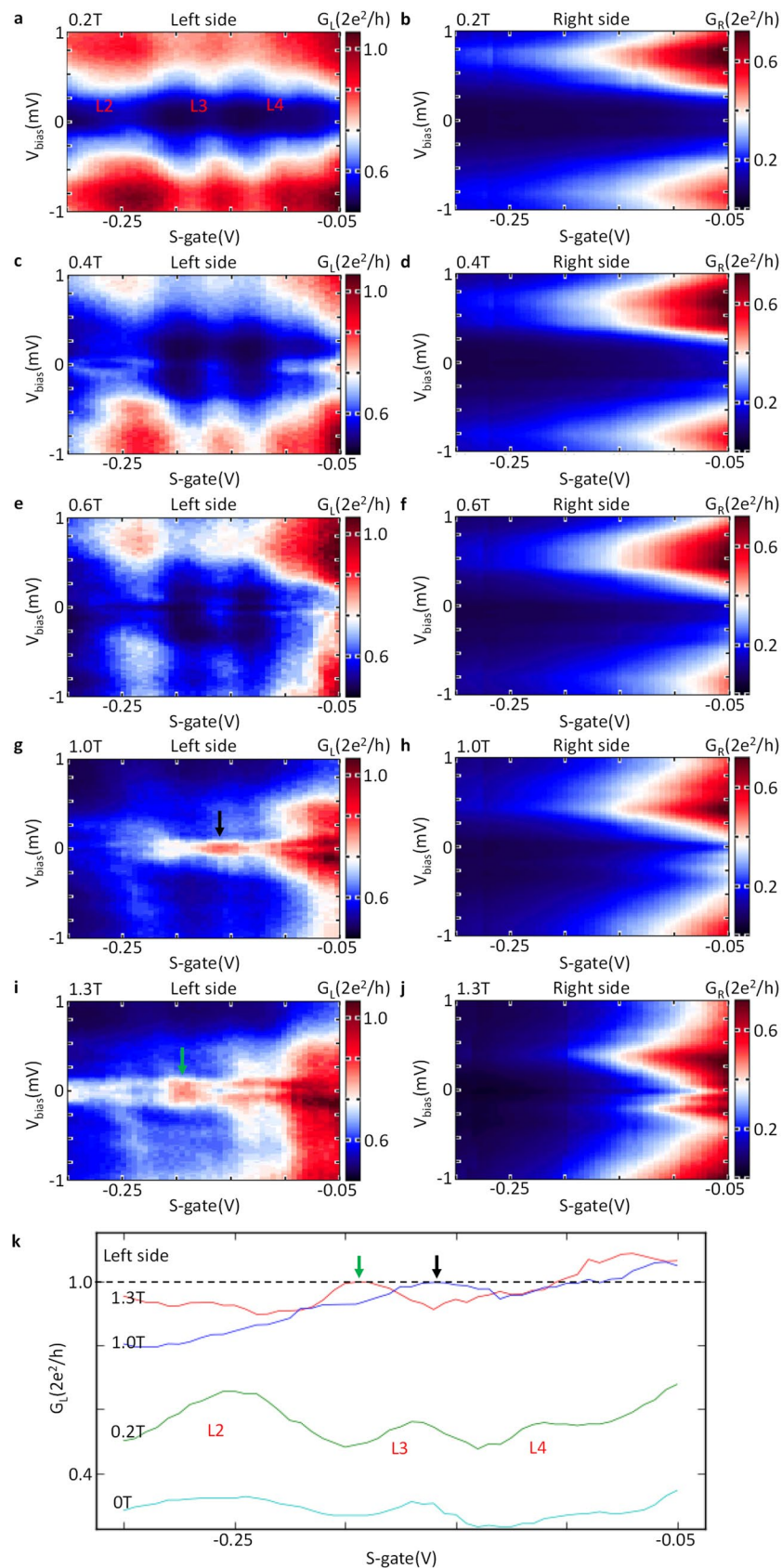
**Extended Data Fig. 1 | Three terminal measurement setups, extended data of the tunnel barrier gate dependence of the ZBCP and the effect of the contact resistance.** **a**, Schematics of the device and measurement setups. Red arrows indicate the direction of dc current flow for positive bias. The source-drain voltage is applied through the superconducting contact, current and differential conductance are measured simultaneously at two normal contacts. The two wider tunnel gates are connected together as T3. **b**, Simplified measurement circuit diagram representing all elements of the circuit as resistors.  $R_{\text{filters}}$  is the resistance of RC filters and  $R_{\text{im}}$  is the input impedance of the current amplifier. Dashed box indicates on chip elements. The nanowire segment in contact with NbTiN is a multi-terminal conductor which can be fully characterized by a resistance tensor,  $R_{\text{Nanowire}}$ , which is the resistance of the nanowire segment between the normal contacts. Semiconductor-normal metal contact resistances are indicated by  $R_{\text{L}}$  and  $R_{\text{R}}$ . The exact values of contact resistances are unknown, but they can be estimated from saturation current at positive gate voltages. **c** and **d**, Differential conductance  $G_{\text{L}}$  and  $G_{\text{R}}$  as functions of  $T_{\text{L}}$  voltage and source-drain voltage from the same dataset as Fig. 2(d). The gate settings are S-gate = -0.17 V and  $T_{\text{R}} = -0.105$  V. **e**, Zero bias linecuts from panel **c** with different  $R'$  subtracted. When 0, 1 k $\Omega$ , 2 k $\Omega$ , 3 k $\Omega$ , 4 k $\Omega$ , 5 k $\Omega$  are subtracted (from bottom to top), the conductance plateau increases from  $0.8 \cdot 2e^2/h$  to  $1.1 \cdot 2e^2/h$ . **f**, Bias linecuts at  $T_{\text{L}} = -0.05$  V (yellow dashed line) from panel **c** and panel **d** show the shape of the ZBCP on the left side and absence of clear ZBCP on the right side.



**Extended Data Fig. 2 | Additional zero field tunnel barrier data and induced gaps.** **a** and **b**, Barrier gate scans from the left and right sides respectively, while S-gate is set to 1 V. The two sides show similar barrier gate dependence and overall transparency. Note the left side reaches  $3 \cdot 2e^2/h$  at saturated regime, indicating a possible contact resistance of 3–4 k $\Omega$ . **c**, Pinch off traces at  $V_{bias} = 10$  mV from panel **a** and panel **b**. **d** and **e**, Differential conductance  $G_L$  and  $G_R$  as functions of S-gate voltage and source-drain voltage, while  $T_L = -0.015$  V and  $T_R = -0.075$  V. While the barrier gates are set near the pinch off regime, the two sides have very similar induced gaps. **f**, Bias linecuts at S-gate = -0.75 V (yellow dashed lines) from panel **d** and panel **e**. The left side has a gap with  $\Delta = 800$   $\mu$ eV and the gap on the right side is about 760  $\mu$ eV. The error bar for the gap estimation is 40  $\mu$ eV.

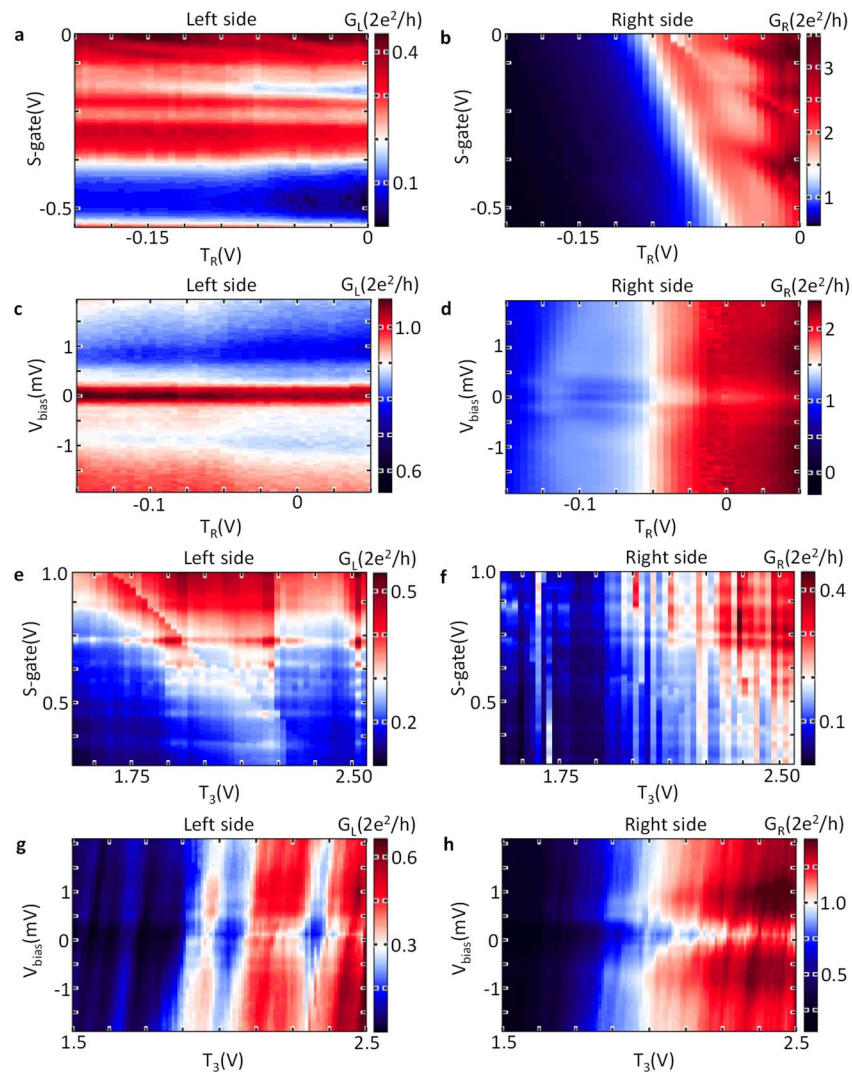


**Extended Data Fig. 3 | Magnetic field angle dependence of the ZBCP and subgap states on both sides.** **a** and **b**, Differential conductance  $G_L$  and  $G_R$  as functions of field angle and source-drain voltage when  $T_R = -0.105$  V,  $T_L = -0.04$  V and S-gate =  $-0.18$  V. Note the contact resistance of  $4$  k $\Omega$  is subtracted for the left side. The field is parallel to the nanowire and perpendicular to the spin-orbit field when the field angle is zero. On the left side, the ZBCP only exists and reaches  $2e^2/h$  within a small angle around zero degree. On the right side, the subgap states are asymmetrical in field angle. Most importantly, no ZBCP is observed in the range  $-20$  degree to  $20$  degree. **c**, Bias linecuts at  $0$ ,  $4$ ,  $-16$  degree field angle from panel **a**. The ZBCP splits into two peaks when the field angle deviates from  $0$  degree. **d**, Zero bias linecuts from panel **a** and panel **b** show distinct behavior on the two sides: the zero bias conductance on the left side peaks at zero degree while the zero bias conductance on the right side remains almost unchanged.

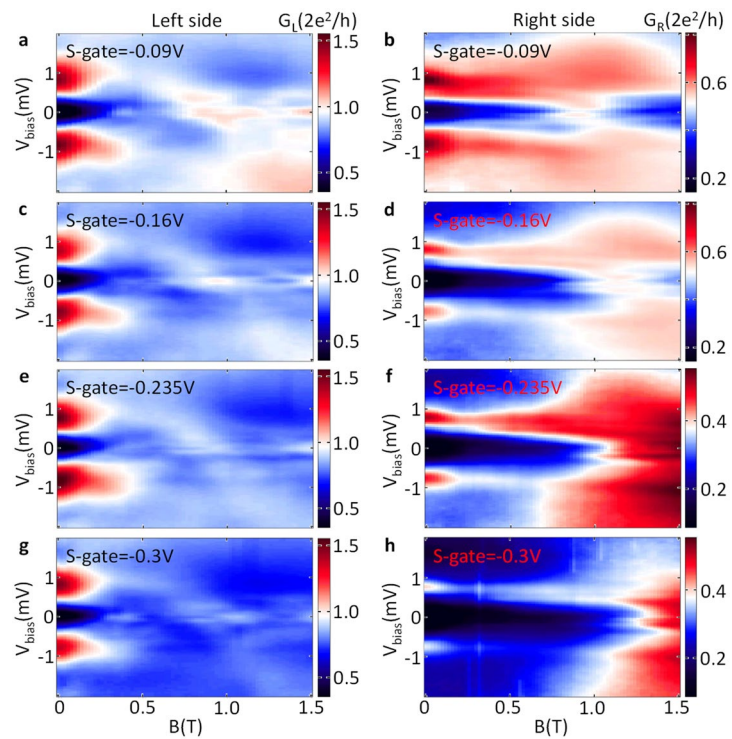


Extended Data Fig. 4 | See next page for caption.

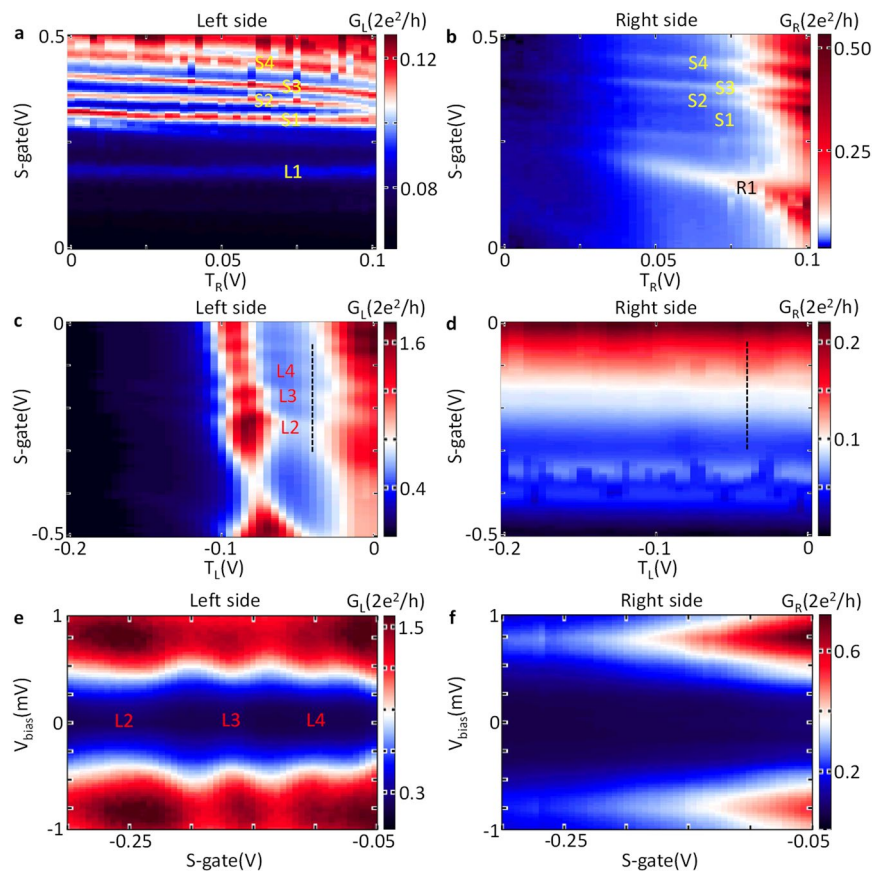
**Extended Data Fig. 4 | Evolution of ZBCPs in magnetic fields. a-j.** Source-drain voltage vs. S-gate scans of the same regime of Extended Data Fig. 7(c)(d) at different fields. The gate settings are  $T_L = -0.045$  V and  $T_R = -0.105$  V. On the left side, subgap states and ZBCPs appear around  $B = 0.3$  T. The height of the ZBCPs reaches  $2e^2/h$  at 1 T (panel **g**) and 1.3 T (panel **i**). The contact resistance of  $4\text{ k}\Omega$  is subtracted for the left side. On the right side, subgap states develop at higher fields. Most importantly, no ZBCP is observed on the right side within the field range investigated. **k**, Zero bias linecuts taken from Extended Data Fig. 7(e), and panels **a**, **g**, **i** show conductance increase with increasing magnetic field and reach  $2e^2/h$  at 1 T and 1.3 T.



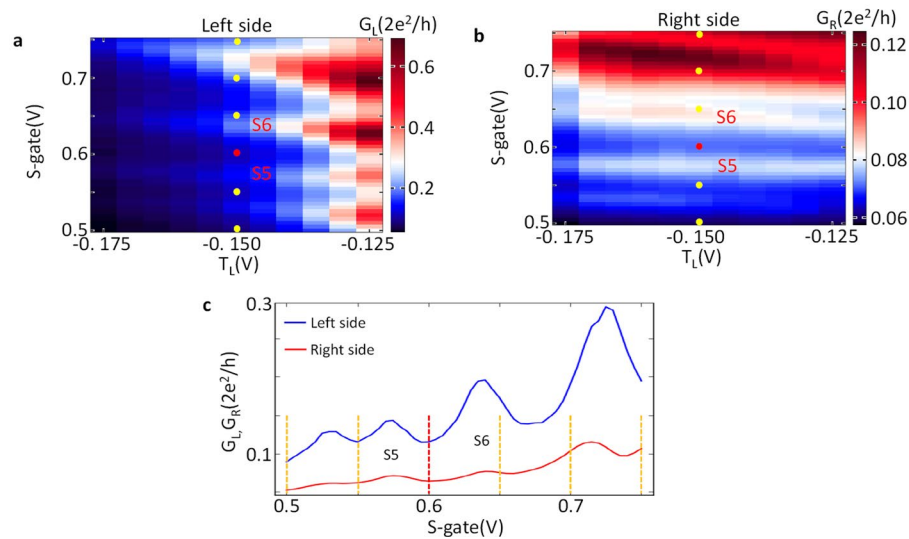
**Extended Data Fig. 5 | Effect of  $T_R$  on the left-side-only ZBCP in Fig. 3 and effect of  $T_3$ .** **a** and **b**, Differential conductance  $G_L$  and  $G_R$  as functions of  $T_R$  voltage and S-gate voltage at zero field and zero bias when  $T_L$  is set to  $-0.04$  V. This is the regime where we find the nearly quantized ZBCP on the left side in Fig. 2. The two sides show distinct states, which confirms the finding that there are only localized states in this regime. **c** and **d**, Differential conductance  $G_L$  and  $G_R$  as functions of source-drain voltage and  $T_R$  voltage at 1 T. While the  $T_R$  pinch off the right side, the ZBCP on the left side remains unchanged with conductance close to  $2e^2/h$ . Notably, there are also states near zero bias on the right side when  $T_R$  is below  $-0.05$  V. However, they never form a ZBCP. The two wider barrier gates are connected and controlled by a single voltage  $T_3$ . For all other measurements in this paper,  $T_3$  is set to above 1.5 V to facilitate high transparency. Here we present the effect of  $T_3$ . **e** and **f**, Differential conductance  $G_L$  and  $G_R$  as functions of S-gate voltage and  $T_3$  voltage at zero bias and zero magnetic field, while S-gate = 1 V,  $T_L = -0.15$  V and  $T_R = 0.1$  V. The resonances we observed in S-gate scans show no considerable gate dependence of  $T_3$ , indicating the associated wavefunctions live far away from  $T_3$ .  $T_3$  also tune different sets of resonances on the left and the right side, which can also be seen in the source-drain voltage vs.  $T_3$  scans (panel **g** and **h**). The gate settings are S-gate = 1 V,  $T_L = -0.1$  V and  $T_R = 0.075$  V. Those states show no considerable gate dependence on S-gate, indicating the existence of more dots above  $T_3$ .



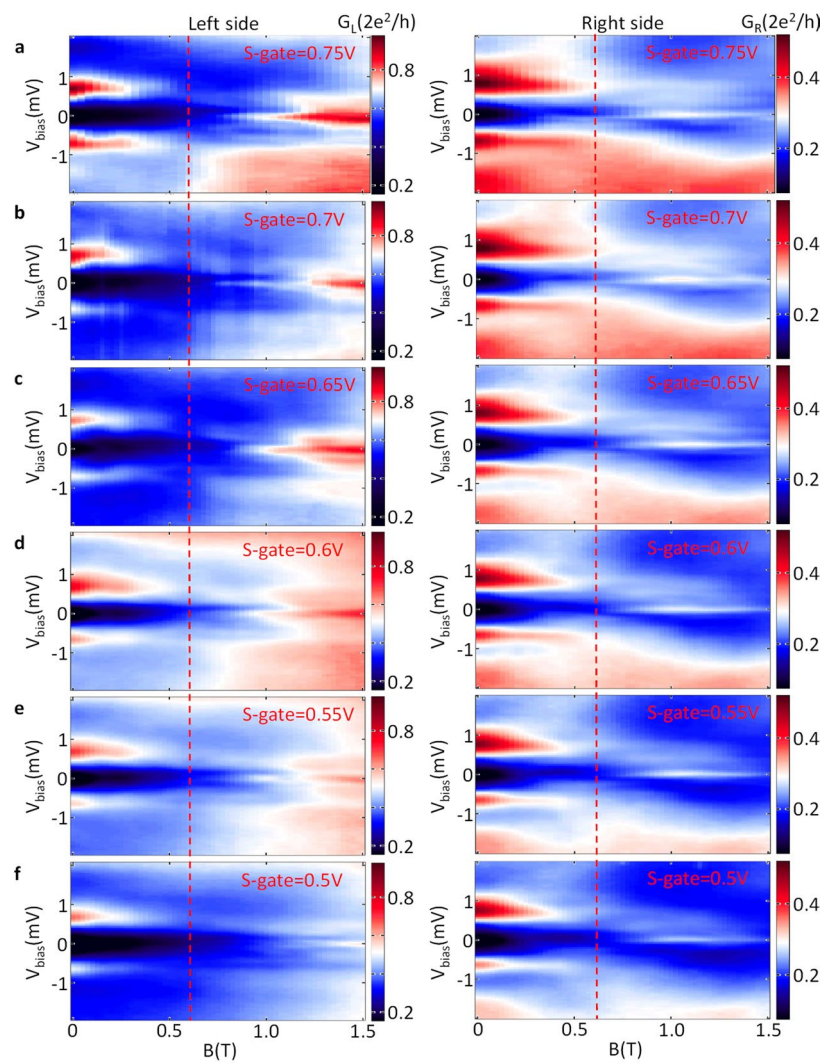
**Extended Data Fig. 6 | Magnetic field dependence of the subgap states for different S-gate voltages.** Magnetic field dependence of the subgap states for different S-gate voltages. Apart from the nearly quantized ZBCP at S-gate = -0.17 V (Fig. 2(a)), we also found similar ZBCPs at S-gate = -0.09 V, S-gate = -0.16 V and S-gate = -0.3 V (panels **a**, **c** and **g**). Only when S-gate = -0.235 V (panel **e**), the ZBCP is lower than  $2e^2/h$ . The tunnel gate settings are  $T_L = -0.045$  V and  $T_R = -0.105$  V. The contact resistance of  $4\text{ k}\Omega$  is subtracted for all the left side scans. On the right side, no correlated ZBCP is observed at any of these S-gate voltages.



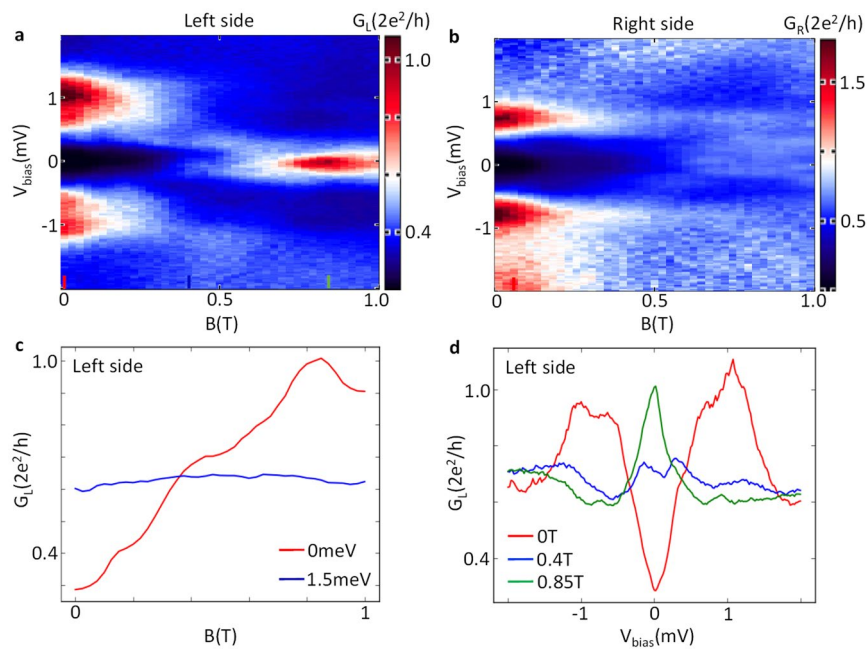
**Extended Data Fig. 7 | Delocalized states vs. localized states in different S-gate regimes.** **a** and **b**, Zero bias differential conductance  $G_L$  and  $G_R$  as functions of  $T_R$  voltage and S-gate voltage (0 V to 0.5 V) at zero magnetic field, while  $T_L$  is set to -0.13 V. On the left side (panel **a**), delocalized states S1-S4 exhibit  $G_R$  dependence, manifesting their non-local property. On the contrary, the localized state L1 shows no  $G_R$  dependence as it does not change with varying  $G_R$  voltage. On the right side (panel **b**), delocalized states S1-S4 appear at the same positions with the same gate dependence as on the left side, while their magnitudes are different on the two sides. The localized state L1 is missing on the right side, which is reasonable as this state is localized near the left side. Similarly, the localized state R1 only appears on the right side. **c** and **d**, Zero bias differential conductance  $G_L$  and  $G_R$  as functions of  $T_L$  voltage and S-gate voltage (-0.5 V to 0 V) at  $B = 0$  T, while  $T_R$  is set to -0.15 V. This is the regime where we find ZBCPs close to quantization on the left side in Fig. 2. While there are three apparent resonances (labeled as L2, L3, L4) on the left side along the black dashed line, no similar features are observed on the right side. These scans confirm the low probability of having well separated Majorana bound states in that region, given the variety of localized and uncorrelated states within the nanowire. **e** and **f**, Source-drain voltage vs. S-gate scans along the black dashed line in panel **c** and panel **d** showing the resonances on the left side and the absence of similar features on the right side.



**Extended Data Fig. 8 | Extended data for regime in Fig. 5.** We have shown ZBCPs onset at similar fields on the left and right sides when S-gate is set to 0.6 V (Fig. 5). As mentioned in the main text, that correlation is not robust against variation in S-gate. In Extended Data Figs. 8 and 9 we present more data around S-gate = 0.6 V. **a** and **b**, differential conductance  $G_L$  and  $G_R$  as functions of  $T_L$  voltage and S-gate voltage at zero field while bias is set to zero and  $T_R = 0.09$  V. The two sides show delocalized states S5 and S6, which can be seen from the two sides simultaneously and have the same gate dependence. Yellow (red) dots indicate the gate setting for Extended Data Fig. 9 (Fig. 5). **c**, S-gate linecuts from panel **a** and panel **b** at  $T_L = -0.15$  V. Yellow (red) dashed lines indicate the S-gate setting for Extended Data Fig. 9 (Fig. 5).



**Extended Data Fig. 9 | Extended data for ZBCPs in Fig. 5.** Here we present more magnetic field scans around the regime of Fig. 5 when  $T_L = -0.15$  V and  $T_R = 0.09$  V. The S-gate settings are indicated by the yellow and red dots in Extended Data Fig. 8. As shown in the left panels, the onset fields of the ZBCPs on the left side change to higher fields when S-gate is reduced. And the ZBCPs also exhibits splitting features at S-gate = 0.55 V and S-gate = 0.5 V. On the right side, however, the ZBCP onset and splitting do not generally match the left side manifestations.



**Extended Data Fig. 10 | Nearly-quantized ZBCP in another S-gate regime.** **a** and **b**, Differential conductance  $G_L$  and  $G_R$  as functions of bias voltage and magnetic field when  $S\text{-gate} = 1\text{ V}$ ,  $T_L = -0.25\text{ V}$  and  $T_R = 0.05\text{ V}$ . This is a regime with a more positive  $S$ -gate setting than that explored in Figs. 1-3. On the left side, a ZBCP appears around  $B = 0.6\text{ T}$  and reaches  $2e^2/h$  around  $0.85\text{ T}$ . The contact resistance of  $4\text{ k}\Omega$  is subtracted for the left side again. While there are some subgap states on the right side around similar fields, no prominent ZBCP is observed. **c**, Magnetic field linecuts at  $V_{\text{bias}} = 0$  and  $V_{\text{bias}} = 1.5\text{ meV}$  from panel **a**. **d**, Bias linecuts at  $B = 0, 0.4\text{ T}$  and  $0.85\text{ T}$  from panel **a**.